Research Article

Diffuse-Double Layer at a Membrane-Aqueous Interface Measured with X-ray Standing Waves

MICHAEL J. BEDZYK, G. MARK BOMMARITO, MARTIN CAFFREY, THOMAS L. PENNER

The ion distribution in an electrolyte solution in contact with a charged polymerized phospholipid membrane was directly measured with long-period x-ray standing waves. The 27-angstrom-thick lipid monolayer was supported on a tungsten/silicon mirror. X-ray standing waves were generated above the mirror surface by total external reflection of a 9.8–kiloelectron volt x-ray beam from a synchrotron undulator. The membrane surface, which contained negatively charged phosphate headgroups, was bathed in a dilute $ZnCl_2$ solution. The concentration of Zn^{2+} in the condensed layer at the membrane surface and the Zn^{2+} distribution in the diffuse layer were measured as a function of headgroup charge. The Debye length of the diffuse layer varied between 3 and 58 angstroms. The results qualitatively agree with the Gouy-Chapman-Stern model.

THE PROPERTIES OF THE INTERFACE FORMED BY AN ELECTrolyte in contact with a charged surface govern a large number of processes, including electrodeposition, colloidal suspension, and ion transport through biological membranes. Due to the separation of charge at such an interface, a gradient in the electrostatic potential, ϕ, arises across the interface which polarizes the solution and affects the ion distribution in the interfacial region. Since the interface resides below a relatively thick aqueous overlayer, high-resolution structure-determining techniques, which rely on charged particle beams or vacuum, cannot be used to profile the ion distribution in the solution immediately above a charged surface. As a consequence, the treatment of this interfacial region has, up until now, been idealized and based on models such as those given by Helmholtz (*1*), Gouy-Chapman (*2*), and Stern (*3*).

X-rays, which can penetrate through millimeters of water, should, in principle, be ideally suited for solving this long-standing problem in electrochemistry. In fact, in situ surface extended x-ray absorption fine structure measurements (*4*) and conventional x-ray standing wave (XSW) measurements (*5*) have been successfully used in determining the bond length distance between a chemically adsorbed atom layer and the surface atom layer at the liquid-solid interface. However, these x-ray techniques, which can be used to measure the distance between atoms that are separated by a few angstroms, cannot be used to measure the ion distribution profile of the diffuse layer that extends tens of angstroms away from the interface.

In this article, we demonstrate how a long-period x-ray standing wave, generated by total external reflection, can be used to directly measure the ion distribution profile in a solution layer above a mirror surface. The most obvious choice for such a demonstration might have been to make the x-ray mirror surface an electrode in an electrochemical cell. However, to show the versatility and power of this new method, we have chosen to measure the ion distribution profile above a charged phospholipid monolayer membrane that has been deposited onto the surface of an x-ray mirror.

This ultrathin organic film is an important model system, since the biological membrane is in essence a bimolecular phospholipid leaflet, in and on which are situated a variety of proteins and other molecules. Such membranes bear fixed charges related to their lipid and protein constituents both of which can be charged. Fixed surface charges are responsible for the electrostatic forces and potentials associated with membranes (*6*). The latter, in turn, are sensitive functions of surface charge density, distance from the surface, and the concentration and identity of ions in the surrounding aqueous medium. Surface electrostatic potentials influence the dynamics and structure of cellular, model, and reconstituted membranes by modulating transport through, ion adsorption to, and interfacial properties of the supporting lipid bilayer (*6*). Given the multifaceted effects of membrane surface charges, the need to

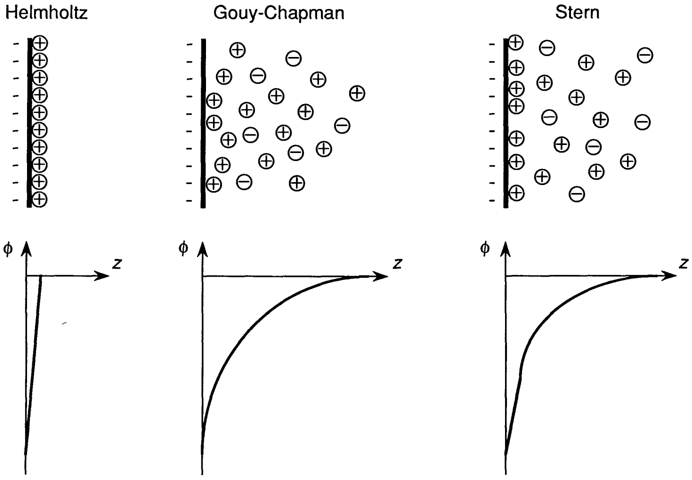

Fig. 1. Models of the electric double layer formed by an ionic solution in contact with a negatively charged surface. Below each model is depicted the distance, z, dependence of the electrostatic potential, ϕ.

M. J. Bedzyk is at the Cornell High Energy Synchrotron Source (CHESS) and The School of Applied and Engineering Physics, Cornell University, Ithaca, NY 14853. G. M. Bommarito is at the Department of Chemistry, Cornell University, Ithaca, NY 14853. M. Caffrey is at the Department of Chemistry, The Ohio State University, Columbus, OH 43210. T. L. Penner is at the Corporate Research Laboratories, Eastman Kodak Company, Rochester, NY 14650.

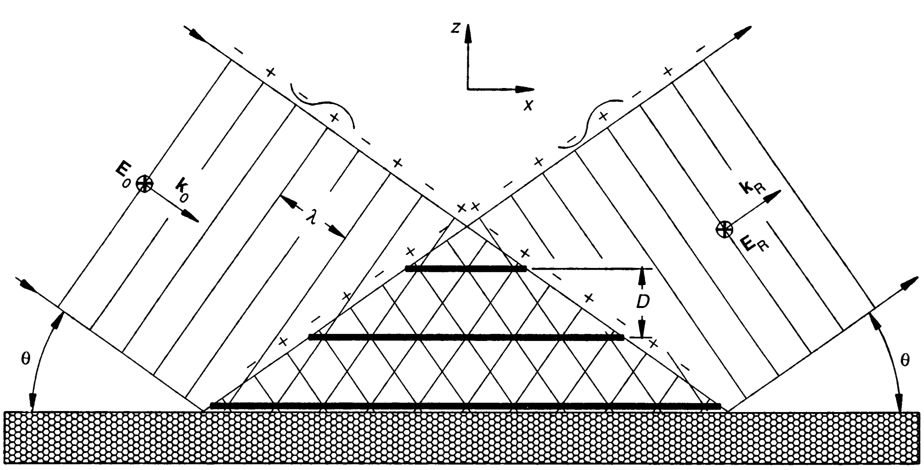

Fig. 2. Illustration of the x-ray standing wave field formed by the interference between the incident, $\mathbf{E}_0$, and specular-reflected, $\mathbf{E}_R$, plane waves above a mirror surface. By locating the intersections of the crests and troughs of the two plane waves, one can easily show that the antinodes of the standing wave are parallel to the mirror surface and have a period of $D = \lambda/2\sin\theta$. Since total external reflection of angstrom-wavelength x-rays occurs at incident angles, θ, which are less than 0.5°, D typically varies between 100 Å and 1000 Å.

characterize the associated electrostatic potential and its consequences is immediately obvious.

The electric double layer. The Helmholtz model (Fig. 1) treats the interfacial region formed by an electrolyte in contact with a charged surface as a parallel-plate capacitor, with one plate containing the surface charge and the other plate, which is referred to as the outer Helmholtz plane, containing electrostatically attracted ions from the solution. The thickness of the double layer is assumed to be the ionic radius. This simplified rigid model of the interface neglects a number of important aspects, such as the thermal motion of the ions.

The Gouy-Chapman model of the diffuse double layer (Fig. 1), which does take into account the thermal motion of the ions, solves the one-dimensional Poisson equation

$$d^2\phi/dz^2 = -\rho/\epsilon \tag{1}$$

for a Boltzmann distribution of ions in thermal equilibrium in a force field which varies in the z-direction perpendicular to the interface. The permittivity of the solution is represented by ϵ (7). The charge density, ρ, which is the sum of the charge densities of the various ion species present in the electrolyte, is

$$\rho(z) = \sum_i N_i c_i e_o = \sum_i N_i^o c_i e_o \exp[-c_i e_o \phi/(kT)] \tag{2}$$

where N_i^o is the bulk concentration of the ith ion species, c_i is the charge valance of the ith ion species, e_o is the elementary charge, k is the Boltzmann constant, and T is the absolute temperature. The concentration of the ith ion species, N_i, at distance z is strictly a function of $\phi(z)$ and T in this model. The potential, $\phi(z)$, in the electrolyte is determined by substituting Eq. 2 into Eq. 1. For a small surface potential, that is, for $e_o\phi << kT$,

$$\phi(z) = \phi_o \exp(-z/L_D) \tag{3}$$

The Debye length, which is related to the thickness of the diffuse layer of ions, is

$$L_D = (\epsilon\, kT/Se_o^2)^{1/2} \tag{4}$$

where $S = \sum_i c_i^2 N_i^o$ is the ionic strength. (For a 0.1 mM $ZnCl_2$ aqueous solution at $T = 25°C$, $L_D = 176$ Å). The surface potential at $z = 0$ is

$$\phi_o = \sigma L_D/\epsilon \tag{5}$$

where σ is the surface charge density.

The Stern model (Fig. 1) extends the Gouy-Chapman model by including specific ion binding at the interface. Here, the first layer of ions is constrained to lie in a Helmholtz plane with a thickness defined by the spherical size of the ions. In general, the condensed or bound layer does not completely neutralize the fixed surface charge, and a diffuse layer exists beyond the interface electrostatically attracted to the residual net surface charge. Ions in the bound layer reduce the surface charge density, σ (Eq. 5), but do not contribute to the electrolyte charge density, ρ (Eq. 2).

X-ray standing waves generated by total external reflection. Referring to Fig. 2, x-rays undergo total external reflection when the incident angle, θ, is less than the critical angle, θ_c. Total external reflection, rather than total internal reflection, occurs because the index of refraction is less than unity for x-rays. The index of refraction is expressed as $n = 1 - \delta - i\beta$, where $\delta = N_e r_e \lambda^2/2\pi$ and $\beta = \mu\lambda/4\pi$. Using Snell's law, $\theta_c = (2\delta)^{1/2}$, which is typically between 1 and 10 mrad, depending on the wavelength, λ, and the effective electron density, N_e. (r_e is the classical electron radius and μ is the linear absorption coefficient.) As previously pointed out (*8, 9*) and recently demonstrated (*10, 11*), the incident and reflected x-ray beams interfere to generate an x-ray standing wave above the reflecting mirror surface. The nodal and antinodal planes of the standing wave are parallel to the mirror surface, and the period of the standing wave is $D = \lambda/2\sin\theta$. Using the Fresnel coefficient for reflection, Bedzyk *et al.* have shown (*11*) that the relative phase between the reflected and incident plane waves at the mirror surface decreases in a continuous fashion from π to 0 when θ is inceased from 0 to θ_c. Thus, at $\theta = 0$ a node coincides with the mirror surface and at $\theta = \theta_c$ an antinode is at the mirror surface. As the mirror is tilted in angle from 0 to θ_c, the first antinode of the standing wave moves inward along the surface normal z-axis from infinity to zero and the remaining antinodes follow behind like a compressing bellows with a period reducing from $D = \infty$ to $D = D_c$. The critical period, $D_c = (\sqrt{\pi}/2)(N_e r_e)^{-1/2}$, which is the period at the critical angle, is 80 Å for a gold mirror and 200 Å for a silicon mirror. For the 3:1 Si/W mirror used in this experiment $D_c = 125$ Å.

The x-ray standing wave is described by the E-field intensity at a distance z above a reflecting interface as

$$I(\theta, z) = |\mathbf{E}_0 + \mathbf{E}_R|^2 \tag{6}$$

where $\mathbf{E}_0$ and $\mathbf{E}_R$ are the incident and reflected traveling E-field plane waves. In the present experimental case, there will be several layers of low-Z material above the Si/W mirror surface. To properly account for the refractive and absorbtive effects, each layer is described by an appropriate thickness and index of refraction. These are then used in Parratt's recursion formulation (*12*) with Fresnel coefficients to calculate the E-field at any position z within any of the layers. For the simplest case involving a single interface, the E-

field intensity in the vacuum above a reflecting mirror surface can be written as

$$I(\theta, z) = |\mathbf{E}_0|^2[1 + R + 2\sqrt{R}\cos(\nu - 2\pi Qz)] \qquad (7)$$

where $|\mathbf{E}_0|^2$ is the intensity of the incident beam, R is the reflectivity, ν is the phase of the reflected beam relative to the incident beam phase, and $Q = 2\sin\theta/\lambda = 1/D$ is the magnitude of the wave vector transfer. Referring to Fig. 2, $\mathbf{Q} = \mathbf{k}_R - \mathbf{k}_0$, where $\mathbf{k}_0$ and $\mathbf{k}_R$ are the wave vectors of the incident and reflected beams, respectively. The intensity, $I(\theta,z)$, modulates between 0 and $4|\mathbf{E}_0|^2$, when $R = 1$.

In the dipole approximation, the photoelectric-effect cross section is proportional to the E-field intensity at the center of an atom. Thus, the position of a layer of atoms above the mirror surface can be determined by monitoring the characteristic x-ray fluorescence yield as the mirror is tilted through the reflection condition. For example, if the atom layer is X critical periods above the mirror surface, then $X + \frac{1}{2}$ modulations in the atom layer's fluorescence yield will occur in a θ scan between 0 and θ_c. This was clearly seen in an earlier study (*11*), where a layer of zinc atoms was suspended in a Langmuir-Blodgett (LB) film 200 Å above a gold mirror surface. In general, the fluorescence yield for an atom (or ion) distribution, $N(z)$, above a mirror surface can be written as

$$Y(\theta) = \int_0^\infty N(z)\, I(\theta,z)\, dz \qquad (8)$$

Since the standing wave samples the selected atom distribution with a variable period, we can, in principle, directly extract the Fourier transform of $N(z)$ from the measured yield, $Y(\theta)$.

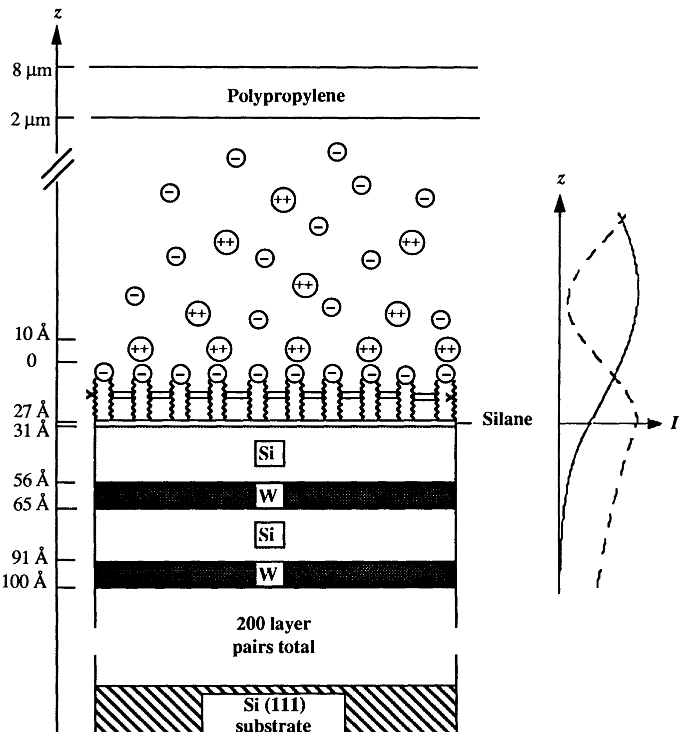

Fig. 3. Schematic showing a cross-linked phospholipid membrane deposited on a silanated Si/W LSM. The top of the phospholipid contains a PO_4^- headgroup which attracts Zn^{2+} ions in the 0.1 mM $ZnCl_2$ aqueous solution. The encapsulating 6-µm-thick polypropylene film traps a 2-µm-thick water layer by capillary action between the film and the phospholipid. Along the right side is shown the E-field intensity at $E_\gamma = 9.8$ keV for $\theta = 2.5$ mrad (solid curve) and $\theta = \theta_c = 4.5$ mrad (dashed curve). When $\theta \leq \theta_c$ an x-ray standing wave exists above the reflecting surface and an evanescent wave exists below.

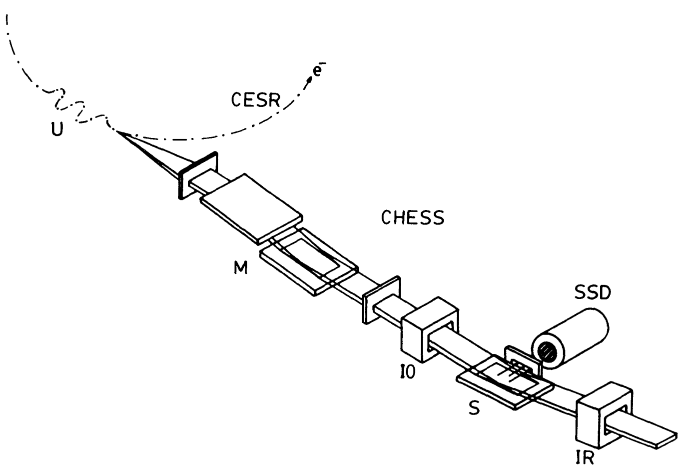

Fig. 4. Experimental setup for collecting x-ray standing wave data. The extremely bright synchrotron x-ray radiation from the undulator (U) is made monochromatic by Bragg diffraction from a Si (111) double-crystal monochromator (M) and then reflected by the sample (S). An x-ray fluorescence spectrum is collected by an energy-dispersive solid-state detector (SSD). The incident and reflected x-ray beam intensities were monitored by ion chambers I0 and IR, respectively.

Experimental description. Referring to the schematic of our sample in Fig. 3, the 27 Å thick phospholipid membrane was deposited from an LB trough containing $ZnCl_2$ onto the surface of a 10 mm wide by 25 mm long silicon-tungsten layered-synthetic-microstructure (LSM). The LB film covered a 10 mm by 15 mm area. To create a uniformly clean and hydrophobic surface, a 4 Å thick dimethysilane layer was adsorbed onto the argon plasma-cleaned Si surface of the LSM prior to the LB film deposition. After deposition, the phospholipid was polymerized by exposure to ultraviolet light. The Zn counterions were them removed from the phospholipid headgroups by a brief rinse in hydrochloric acid. X-ray fluorescence was used to verify that all of the Zn had been removed. The sample was then enclosed in a Teflon cell with a 6-µm-thick polypropylene window drawn across the top of the wet sample surface. After extensive rinsing with a 0.1 mM $ZnCl_2$ aqueous solution at a pH of 6.8, a slight negative pressure was applied to the cell to reduce the thickness of the aqueous layer above the mirror to ~2 µm for the XSW measurements. The aqueous layer and the polypropylene thickness were measured by x-ray reflectivity. After completing the XSW measurement at pH 6.8, a fresh 0.1 mM $ZnCl_2$ solution of a lower pH (adjusted with HCl) was used to extensively rinse the sample and was used in the subsequent measurement. A complete XSW measurement incorporated a scan in angle, θ, through the total external reflection condition and a scan in θ through the first order Bragg reflection of the Si/W LSM which had a period of $d = 35$ Å ($d_{Si} = 26.25$ Å and $d_W = 8.75$ Å). Only the results from the scans through the total external reflection is discussed in this article.

Referring to Fig. 4, the experiment was carried out at the Cornell High Energy Synchrotron Source (CHESS) with x-rays from the second harmonic of a 123-pole undulator (*13*) with the Cornell Electron Storage Ring (CESR) operating in a low emittance mode at an energy of 5.44 GeV and a beam current of 35 to 55 mA. Light from this high brightness source was monochromated by a pair of Si(111) crystals to a photon energy of $E_\gamma = 9.8$ keV for optimally exciting Zn K fluorescence. The first Si crystal incorporated liquid gallium cooling (*14*) into its design to handle the enormous heat density from the undulator. Both the monochromator and the sample were set up to reflect into the vertical plane. The sample surface was exposed to an incident beam of 8×10^8 photons per second with a slit width of 0.88 mm and a height of 20 μm. An energy-dispersive solid-state detector was positioned perpendicular to the incident and reflected beams to collect the fluorescence at a glancing angle with respect to the sample surface. Each scan consisted of 64 equally spaced steps in angle between 0 and 10 mrad. At each step a 256-channel fluorescence spectrum was collected along with the incident and reflected beam intensities which were monitored by ion chambers. The *p*H 6.8 data required 4 seconds per step.

Experimental observations. The simultaneously collected reflectivity and Zn Kα fluorescence data for the initial scan at *p*H 6.8 are shown in Fig. 5, A and B, respectively. The drop in reflectivity for $\theta < 0.8$ mrad is due to the 20-μm incident beam height oversubtending the 25-mm length of the sample. For an ideal simple mirror the reflectivity is nearly 100 percent for angles less than θ_c and drops off precipitously for $\theta > \theta_c$. The first drop off in reflectivity at 1.8 mrad corresponds to the critical angle for polypropylene and water at 9.8 keV (both materials have roughly the same electron density, thus the same θ_c). The drop off in reflectivity at 4.5 mrad corresponds to θ_c for a 3:1 mixture of Si/W. Since the polypropylene film is not perfectly flat, the maximum reflectivity from the polypropylene is only 60 percent. The measured absolute reflectivity at 3 mrad is only 32 percent owing to the attenuation of both the incident and reflected beams by the 6-μm-thick polypropylene film and the 2-μm-thick water layer. At 3 mrad this corresponds to a total traversed length through 4 mm of polypropylene and 1.3 mm of water. With a linear absorption coefficient of 1.6 cm^{-1} for polypropylene and 5.0 cm^{-1} for water, the transmission factors for the polypropylene and the water are 0.53 and 0.52, respectively. The product of the two factors is 0.28, which is slightly less than the measured 0.32. This means that the water was actually 1.5 μm thick during this scan, rather than the nominal 2 μm. The calculated reflectivity in Fig. 5A has much sharper features than the measured data because the calculation is based on a model which neglects interfacial roughness and slope errors. This is of significance primarily in the lower angle region where the air/polypropylene interface imperfections reduce the reflectivity for $\theta < 2$ mrad and also reduces the antireflectivity effect (*15*) around 3 mrad. Such effects are of little consequence in the present fluorescence yield analysis, since it will be primarily based on data points taken above the polypropylene critical angle.

The Zn Kα fluorescence count rate shown in Fig. 5B is very low for θ smaller than the polypropylene critical angle of 1.8 mrad. This is related to the fact that the incident x-ray traveling wave is forbidden to penetrate through a mirror surface during total external reflection. Keeping in mind that the first antinode moves inward toward the Si/W mirror surface as the angle is advanced toward the Si/W critical angle, notice that the first XSW antinode passes over the maximum of the Zn density before the Si/W critical angle is reached. This indicates that a concentrated layer of Zn exists at some displaced distance above the Si/W surface (see Fig. 3). If, for example, the phospholipid had been inadvertently stripped away, and the Zn formed an atom plane in immediate contact with the Si/W mirror, the Zn signal would peak at the Si/W critical angle.

Unlike the *p*H 6.8 data, the *p*H 4.4 and *p*H 2.0 Zn fluorescence yield curves shown in Fig. 5, C and D, do not diminish strongly below the polypropylene critical angle. This is due to a small amount of Zn^{2+} passing into the partially hydrolized polypropylene.

The off-reflection Zn fluorescence yield at $\theta = 10$ mrad is a very useful indicator of the total amount of Zn in the system. By comparing the off-reflection yields in Fig. 5, B and C, we see that the total amount of Zn reduces as the hydrogen ion concentration increases.

Comparison of the data to the electric double-layer models. As can be seen in Fig. 5B, the calculated fluorescence yield based on the Helmholtz model (dashed line) is inconsistent with the *p*H 6.8 experimental data. Whereas, the calculated fluorescence yield for a Zn^{2+} distribution with an exponential decay function form, which is

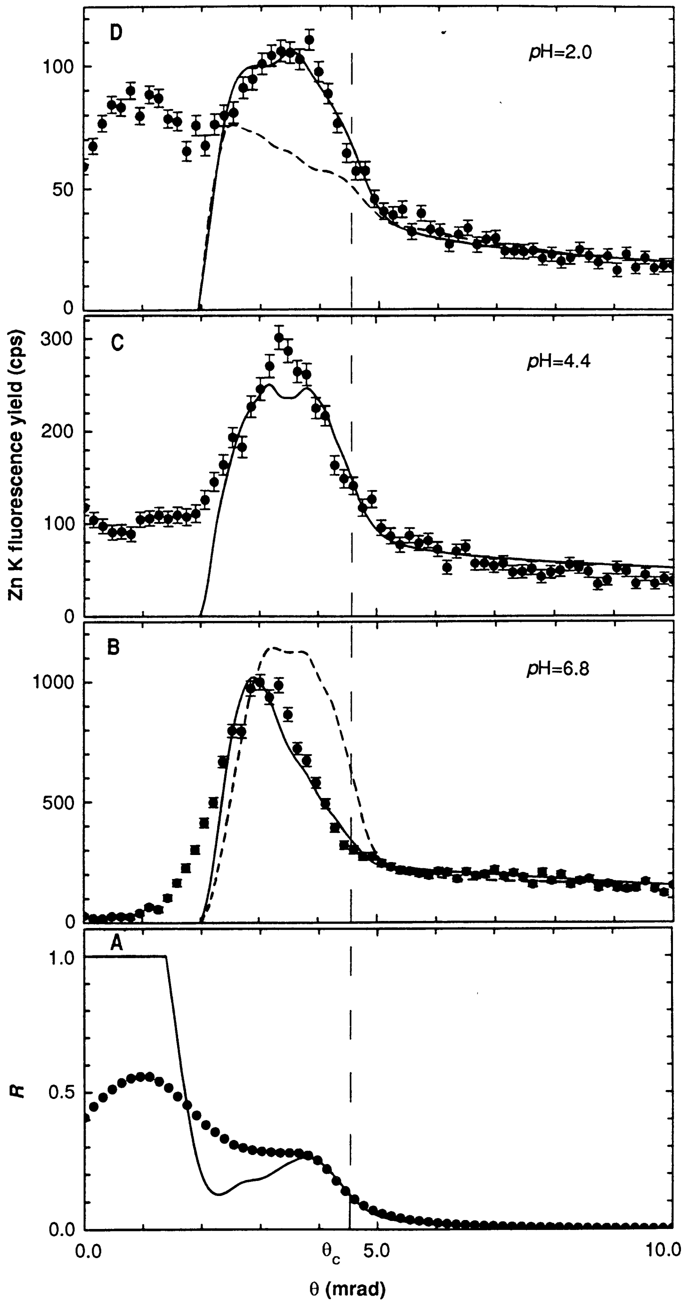

Fig. 5. The experimental (circles) and theoretical (solid lines) angular dependence at $E_\gamma = 9.8$ kev of (**A**) the specular reflectivity and (**B–D**) the Zn Kα fluorescence yield for (B) *p*H 6.8, (C) *p*H 4.4, and (D) *p*H 2.0. The best χ^2 fitted curves (solid line) in (B) to (D) correspond to Eqs. 8 and 9 with values from Table 1. The dashed curve in (B) corresponds to the Helmholtz model with $L' = 0$ and the dashed curve in (D) corresponds to a constant Zn^{2+} distribution with $N_c = 0$. The reflectivity values and angle positions were measured directly on an absolute scale. The count rate of the Zn Kα yields were normalized to the same incident flux of 8×10^8 photons per second. The net Zn Kα counts at each angle were determined by a χ^2 fit of a Gaussian curve on a linear background to the Zn Kα peak in the fluorescence spectrum. The error bars in (B) to (D) correspond to the standard deviation of the Gaussian curve area.

qualitatively based on the Gouy-Chapman-Stern model, agrees well with the data. For the Helmholtz model a half monolayer of Zn^{2+} ions completely neutralizes the PO_4^- monolayer and forms a discrete layer at $z = 2$ Å (see Fig. 3). For the exponential decay distribution the calculated yield in Eq. 8 has a Zn^{2+} ion distribution,

$$N(z) = N_c \exp(-z/L') + N^0, \text{ for } 0 < z < 1.5 \ \mu\text{m} \qquad (9)$$

Based on the best χ^2 fit of Eq. 8 to the data shown in Fig. 5B, our measurement shows that the Zn concentration of the condensed surface layer is $N_c = 0.31M$ and the Debye length of the Zn^{2+} ion distribution is $L' = 58$ Å. The ion Debye length, L', and the potential Debye length, L_D, are equivalent only when the surface potential is weak and the electrolyte is dilute. In our case the electrolyte is dilute, but the surface potential is not weak ($e_o\phi_o \simeq kT$). Therefore, L' should be less than $L_D = 176$ Å.

The computer model used in this calculation was composed of a series of 4 Å thick layers with concentrations in atoms per square centimeter based on Eq. 9. Therefore, the surface concentration of $N_c = 0.31M$ actually corresponds to a coverage of 7.71×10^{12} Zn atoms per square centimeter. With a surface area of 40 Å^2 per phospholipid molecule this corresponds to a Zn coverage of 0.48 monolayer. Using known bulk rate constants (*16*) for the formation of the lipid-zinc complex LZn^{1+} and the mass-action law, we calculated that the fractional condensation should be 0.46, that is, 46 percent of the phospholipid molecules (L^{1-}) are bonded to a Zn^{2+} ion making an LZn^{1+} complex and the remaining 54 percent exist free as L^{1-}. The rate constant for producing L_2Zn^0 is much lower and was therefore neglected. Comparing the measured coverage 0.48 monolayer to the calculated fractional condensation of 0.46 indicates that the Zn at the surface exists in a condensed state rather than in an electrostatically attracted state. A summary of the measured N_c and L' values for subsequent XSW scans at lower pH values is given in Table 1. The model for the Zn^{2+} ion distribution described by Eq. 9 was used in each case. As expected from Eq. 4, the Debye length decreases significantly as the H^+ concentration, and thus, the ionic strength, S, increases. The condensed Zn layer concentration is affected much less by the increased H^+ concentration than is the electrostatically attracted Zn^{2+} ion concentration in the diffuse layer.

By comparing the differences between the various yield curves in Fig. 5, B to D, which correspond to various Zn distributions, it is apparent that this newly developed long-period XSW method is sensitive to subtle changes in the ion distribution at a charged liquid-solid interface. To further illustrate this point, look at the yield curve in Fig. 5D that was calculated for a constant Zn^{2+} distribution, that is, for $N_c = 0$ in Eq. 9. This curve and that calculated for $L' = 0$ in Fig. 5B represent measurable responses for the two extreme cases of the Gouy-Chapman-Stern diffuse–double layer model.

Such a direct measurement of the ion distribution above a charged surface at this level of sensitivity has not heretofore been possible (*17*). At this stage, the method is limited to measuring distributions of ions with x-ray fluorescence energies high enough to penetrate through the outer water layer and encapsulating plastic film. It should also be pointed out that it was important to make the total amount of Zn in the interfacial region large in comparison to the total volume of Zn in the remaining 2 μm of solution. Otherwise, the Zn fluorescence yield data scans would have been undistinguishable from the constant Zn distribution yield curve shown in Fig. 5D.

Table 1. X-ray standing wave measured values of the Zn^{2+} excess surface concentration, N_c, and Debye length, L', for different pH levels. The listed values and standard deviations for N_c and L' were determined by a χ^2 fit of Eqs. 8 and 9 to the data shown in Fig. 5, B to D.

pH	N_c (M)	L'(Å)
6.8	0.31 ± 0.04	58 ± 4
4.4	0.31 ± 0.02	8 ± 2
2.0	0.18 ± 0.02	3 ± 1

Conclusion. We have demonstrated how long-period x-ray standing waves can be used to directly measure the ion distribution profile in an electrolyte solution in contact with a charged surface. The measurements show a qualitative agreement with the Gouy-Chapman-Stern model which predicts that the charged surface can be partially neutralized by a condensed (or adsorbed) layer of counterions and that the ion distribution in the solution will form a diffuse layer with an exponential decay functional form.

REFERENCES AND NOTES

1. H. L. F. von Helmholtz, *Ann. Physik* **89**, 211 (1853).
2. G. Gouy, *J. Phys. Radium* **9**, 457 (1910); D. L. Chapman, *Phil. Mag.* **25**, 475 (1913).
3. O. Stern, *Z. Elektrochem.* **30**, 508 (1924).
4. L. Blum *et al.*, *J. Chem. Phys.* **85**, 6732 (1986).
5. P. L. Cowan, J. A. Golovchenko, M. F. Robbins, *Phys. Rev. Lett.* **44**, 1680 (1980).
6. S. McLaughlin, *Annu. Rev. Biophys. Chem.* **18**, 113 (1989).
7. At 25°C the permittivity of water is $\epsilon = 78\epsilon_o$, where ϵ_o is the permittivity of vacuum.
8. R. S. Becker, J. A. Golovchenko, J. R. Patel, *Phys. Rev. Lett.* **50**, 153 (1983).
9. M. J. Bedzyk, *Nucl. Instr. Methods* **A266**, 679 (1988).
10. ______, D. H. Bilderback, G. M. Bommarito, M. Caffrey, J. S. Schildkraut, *Science* **241**, 1788 (1988).
11. M. J. Bedzyk, G. M. Bommarito, J. S. Schildkraut, *Phys. Rev. Lett.* **62**, 1376 (1989).
12. L. G. Parratt, *Phys. Rev.* **95**, 359 (1954).
13. D. H. Bilderback *et al.*, *Rev. Sci. Instrum.* **60**, 1419 (1989).
14. R. K. Smither *et al.*, *ibid.*, p. 1486.
15. In the vicinity of 3 mrad, the reflected beam from the air/polypropylene interface interferes destructively with the reflected beam from the SiW mirror surface.
16. A. E. Martell and R. M. Smith, *Critical Stability Constants* (Plenum, New York, 1977).
17. Another, recently developed x-ray reflectivity method, called near total external fluorescence (NTEF), has recently been used to investigate the accumulation of metal ions at an LB film/aqueous interface [J. M. Bloch *et al.*, *Phys. Rev. Lett.* **61**, 2941 (1988)]. With this method surface fluorescence is enhanced by the evanescent wave which exists below the reflecting surface. NTEF is useful for studying the ion distribution below a floating membrane, but is less structurally sensitive than the long-period XSW method, since it uses the angle θ dependence of the exponentially damped E-field intensity below the reflecting surface, rather than the more dramatic and phase-sensitive θ dependence of the standing wave which exists above the reflecting surface. See right-hand side of Fig. 3.
18. We thank the CHESS staff, J. S. Schildkraut, R. K. Smither, M. McMillan, H. D. Abruña, and J. H. White for technical help, and B. W. Batterman, D. H. Bilderback, and K. Finkelstein for reading the manuscript. This experiment was made possible by a 1-month dedicated run at CESR. The undulator project was carried out jointly by CHESS and Argonne National Laboratory. We thank the accelerator staff at CESR for their efforts in reconfiguring the storage ring to meet undulator requirements. Supported by the U.S. National Science Foundation under grants DMR-87-19764 and CHE-87-05769, by the U.S. National Institutes of Health under grant DK-36849, by the U. S. Department of Energy under contract W-31-109-ENG-38, and by the College of Agriculture and Life Science at Cornell.

26 January 1990; accepted 2 March 1990